Development 137, 2579-2585 (2010) doi:10.1242/dev.051326


# MEX-5 enrichment in the *C. elegans* early embryo mediated by differential diffusion

**Brian R. Daniels[1], Terrence M. Dobrowsky[1], Edward M. Perkins[2], Sean X. Sun[1,3] and Denis Wirtz[1,3,*]**

## SUMMARY

Specification of germline and somatic cell lineages in *C. elegans* originates in the polarized single-cell zygote. Several cell-fate determinants are partitioned unequally along the anterior-posterior axis of the zygote, ensuring the daughter cells a unique inheritance upon asymmetric cell division. Recent studies have revealed that partitioning of the germline determinant PIE-1 and the somatic determinant MEX-5 involve protein redistribution accompanied by spatiotemporal changes in protein diffusion rates. Here, we characterize the dynamics of MEX-5 in the zygote and propose a novel reaction/diffusion model to explain both its anterior enrichment and its remarkable intracellular dynamics without requiring asymmetrically distributed binding sites. We propose that asymmetric cortically localized PAR proteins mediate the anterior enrichment of MEX-5 by reversibly changing its diffusion rate at spatially distinct points in the embryo, thus generating a stable concentration gradient along the anterior-posterior axis of the cell. This work extends the scope of reaction/diffusion models to include not only germline morphogens, but also somatic determinants.

**KEY WORDS: *C. elegans*, FCS, FRAP, MEX-5, Live-cell microscopy, Protein diffusion**

## INTRODUCTION

A common mechanism of generating cellular diversity in developing organisms is oriented asymmetric cell division, in which cell fate is determined through heterogeneous intracellular endowment, as opposed to the extracellular position-dependent cues of the induction mechanism. In order for daughter cells to inherit distinct intracellular determinants, precursor cells must establish and maintain polarized intracellular domains such that cellular division generates unique daughter cells (Betschinger and Knoblich, 2004; Cuenca et al., 2003; Grill et al., 2001). The physical mechanisms responsible for the formation of intracellular spatial domains remain poorly understood. Cytoplasmic gradients established in embryogenesis have conventionally been explained by hypothetical generation/degradation mechanisms (Crick, 1970; Gregor et al., 2007; Tostevin and Howard, 2008). However, recent reports suggest that multiple cytoplasmic proteins are enriched to opposite ends of the *C. elegans* zygote by related mechanisms in which generation and degradation do not play a role (Daniels et al., 2009; Tenlen et al., 2008). The germline determinant PIE-1 is enriched in the posterior cytoplasm, whereas the somatic cell-fate determinant MEX-5 is enriched in the anterior cytoplasm of the early embryo. In both cases, it has been shown that the enriched proteins appear to be diffuse throughout the zygote, that compartmentalization does not play a role, and that the bulk diffusion rates of each protein are decreased in the respective regions of enrichment. Despite the high similarity of MEX-5 and PIE-1 enrichments, two fundamentally different models of polarized protein segregation have been proposed (Daniels et al., 2009; Tenlen et al., 2008). Here, we reconcile these two models based on experimental findings from both groups, and present additional data supporting MEX-5 enrichment by differential diffusion.

Recently, we reported that the PIE-1 posterior enrichment is maintained by a binary cycling of PIE-1 between two forms with unequal diffusion coefficients. Briefly, the forward reaction (fast → slow) occurs heterogeneously in the posterior of the zygote, whereas the reverse reaction (slow → fast) occurs homogeneously in the cytoplasm (Daniels et al., 2009). This model predicts a stable concentration gradient enriched in the vicinity of the heterogeneous posterior reaction surface and is consistent with the unusual diffusion behavior measured by fluorescence recovery after photobleaching (FRAP) and fluorescence correlation spectroscopy (FCS) of PIE-1 in vivo. The model predicts gradients in both the bulk diffusion rate and the ratio of fast to slow protein across the anterior-posterior (A/P) axis of the zygote, with the slowly diffusing PIE-1 making up a higher proportion of the diffusing protein in the posterior germplasm (Daniels et al., 2009). Live-cell fluorescence microscopy data strongly suggested the presence of at least two distinct species of PIE-1 in relative ratios that were consistent with theoretical predictions of the model.

It has recently been shown that MEX-5 asymmetry requires PAR-4- and PAR-1-dependent phosphorylation, which causes an increase in the bulk diffusion rate of MEX-5 in the posterior (i.e. the depleted side) of the zygote (Tenlen et al., 2008). The proposed speculative 'actomyosin binding model' for MEX-5 enrichment suggests that protein enrichment is mediated via an asymmetrically distributed network of microfilaments, to which MEX-5 can bind. Tenlen et al. (Tenlen et al., 2008) speculated that the binding of MEX-5 might be modulated by posteriorly localized PAR-1, which presumably decreases the binding affinity between MEX-5 and actomyosin in the posterior, resulting in an increase in the effective diffusion rate of MEX-5. However, this model appears to be inconsistent with published data that show that phosphorylated MEX-5 [MEX-5(pS458)] becomes enriched in the anterior of the zygote, where bulk diffusion rates are in fact decreased (Tenlen et

[1]Department of Chemical and Biomolecular Engineering, [2]Integrated Imaging Center and [3]Johns Hopkins Physical Sciences in Oncology Center, The Johns Hopkins University, Baltimore, MD 21218, USA.

*Author for correspondence (wirtz@jhu.edu)

**Accepted 18 May 2010**

al., 2008). Specifically, it is unclear why phosphorylated MEX-5, with its presumed low binding affinity, would become enriched in a region with a high density of putative binding sites. It is also unclear why phosphorylated MEX-5, with an increased rate of diffusion, would be enriched in a region of the zygote that exhibits an overall decreased rate of diffusion. Furthermore, it is not understood why PAR-1 must be properly localized to the posterior cortex of the zygote for proper enrichment of MEX-5 in the anterior cytoplasm.

Using a combination of live-cell imaging and mathematical modeling, we investigate the intracellular dynamics of MEX-5 and propose a differential-diffusion model for the asymmetric enrichment of MEX-5 in the *C. elegans* early embryo that is consistent with all available data.

## MATERIALS AND METHODS

### *C. elegans*

The MEX-5::GFP *Caenorhabditis elegans* strain used in this study (JH1448; axEx1125[pKR2.04 + pRF4 + mex-5::GFP]; *mex-5* in the pKR1.42 *pie-1* vector) was generously provided by Geraldine Seydoux (Johns Hopkins University, Baltimore, USA) and cultured as described previously (Brenner, 1974; Daniels et al., 2006), except that it was maintained at 25°C. Expression patterns were consistent with those described previously (Cuenca et al., 2003).

### Quantitative live-cell fluorescence microscopy

For imaging of embryos (except FCS, see below), worms were dissected and imaged in egg salts (118 mM NaCl, 121 mM KCl, in water) and their embryos were transferred to 3% (w/v) agarose pads (Invitrogen, Carlsbad, CA, USA) that were then sealed by capillary action beneath glass coverslips (VWR, West Chester, PA, USA). We collected fluorescent images of individual embryos with an LSM 510 META scanning confocal microscope with a Plan Apochromat 100× 1.4 NA DIC oil-immersion lens (Zeiss, Germany), using 1.2 scan zoom and 512×512 resolution. The microscope was controlled using Zeiss LSM acquisition software (version 4.2). GFP was excited at 488 nm using the argon laser. Fluorescence intensity was quantified using Zeiss LSM Image Examiner software. All embryos were monitored until at least the 8-cell stage to ensure viability. The imaging acquisition temperature was maintained at 25°C using an ASI 400 stage warmer (Nevtek, Burnsville, VA, USA), except for FCS which was performed at room temperature. Figures were assembled in Adobe Illustrator with only linear adjustments to intensity.

### Fluorescence recovery after photobleaching (FRAP)

We photobleached various regions of interest (ROIs) within individual embryos at pronuclear meeting (avoiding subcellular organelles, such as visible P granules, centrosomes and pronuclei) and monitored the subsequent fluorescence recovery within the photobleached region. All photobleaching was carried out using a Zeiss LSM 510 META with Plan Apochromat 100× 1.4 NA DIC oil-immersion objective, 100% laser power at 488 nm, with 70 iterations and 5.12 μs pixel time in each ROI. The microscope was controlled using the Zeiss LSM acquisition software (version 4.2). Images of photobleached embryos were acquired immediately prior to, and continuously after, photobleaching using the image acquisition settings and laser output power described in the above section. Our specified ROIs for FRAP analysis were 4.5 μm diameter circles.

### Fluorescence correlation spectroscopy (FCS)

We performed FCS as previously described (Daniels et al., 2009). Embryos were dissected in egg salts and transferred to WPI FD35 coverglass-bottom culture dish (World Precision Instruments, Sarasota, FL, USA) containing egg salts. Measurements were collected using the 488 nm argon laser line and a C-Apochromat 40×/1.2 NA W Corr water-immersion objective mounted on an LSM 510 Confocor 3 microscope equipped with Avalanche photodiodes (Carl Zeiss, Germany). For each embryo, we collected five sequential measurements (10 seconds each) from anterior and posterior positions selected using an image captured immediately before measurement and positioned with the scanning mirrors. We chose positions in the cytoplasm away from the pronuclei and the cell cortex. The confocal volume was calibrated using freely diffusing Rhodamine Green succinimidyl ester (Invitrogen) and the data were collected and analyzed with the LSM 510/Confocor software (version 4.2). Our system parameters were determined to be V (confocal volume)=0.17 fl, S (structural parameter)=5.53 and $\omega_{xy}$ (beam radius)=0.17335591.

The autocorrelation data presented were fitted using models of multiple freely diffusible components with Zeiss Confocor 4.2 software for time-lags between 16 μs and 183.5 mseconds. Owing to the fact that MEX-5 is known to associate with granules that exhibit irregular size and shape, autocorrelation was ignored at longer time-lags in order to reduce the heterogeneity expected for this slowly diffusing species. The first scan of each set of five scans was omitted from the analysis owing to bleaching of immobile elements evident in the photon counts.

### FEM analysis

Multi-dimensional solutions to the partial differential equations governing the model described here were obtained using COMSOL v3.5a Multiphysics (FEMLAB) software (Reddy, 1993; Sun et al., 2009). Embryos were simulated using an oval shape with major and minor axes of 50 μm and 30 μm, respectively. The embryonic center was defined as the origin, with the anterior half of the embryo defined where $x<0$ and the posterior defined where $x>0$. To converge on a solution to the governing equations, the concentration of the rapidly diffusing species, $A$, was set to equal unity at the apex of the anterior division ($x=-25$ μm) (see Appendix S1 in the supplementary material).

### Statistics

The number of embryos examined for each experiment is indicated in the figure captions. Calculation of mean and s.e.m. and statistical analyses were performed using Excel (Microsoft, Redmond, WA, USA) and plotted using Prism (GraphPad Software, San Diego, CA, USA). F-tests were conducted to determine whether FCS data were best represented by single- or multi-component models. Two-tailed unpaired *t*-tests were conducted to determine significance in photobleaching data.

## RESULTS

### MEX-5 exists as multiple diffusional species in the early *C. elegans* embryo

In order to characterize the diffusion of MEX-5::GFP in the early embryo, we used various live-cell fluorescence microscopy methods. We used fluorescent recovery after photobleaching (FRAP) to probe the diffusion behavior of MEX-5::GFP within the zygote and fitted the resulting curves to simple one- and two-component recovery models. We photobleached 4.5 μm diameter circular regions of interest in the cytoplasm of embryos expressing MEX-5::GFP with minimal bleaching times (Fig. 1A). Although short bleaching times yield relatively shallow bleach depths, they avoid artifacts in FRAP that can arise when molecules exchange between the region of interest and the bulk cytoplasm during the photobleaching period. Analytical one-component FRAP yielded best-fit recovery half-times of 3.3 and 2.1 seconds in the anterior and posterior, respectively (Fig. 1B,C), which is consistent with previous findings that recovery takes place more slowly in the anterior than posterior of the cell (Tenlen et al., 2008). Because the effective viscosity is symmetric (Daniels et al., 2006; Tenlen et al., 2008), these differences in recovery are not due to a global difference in cytoplasm between anterior and posterior regions. This single-component recovery model predicted immobile fractions of 8% and 4% within the anterior and posterior, respectively. However, we found that the recovery half-times and immobile fractions depended on the time spans used for data fitting (data not shown), which suggests that one-component recovery does not accurately describe these FRAP experiments.

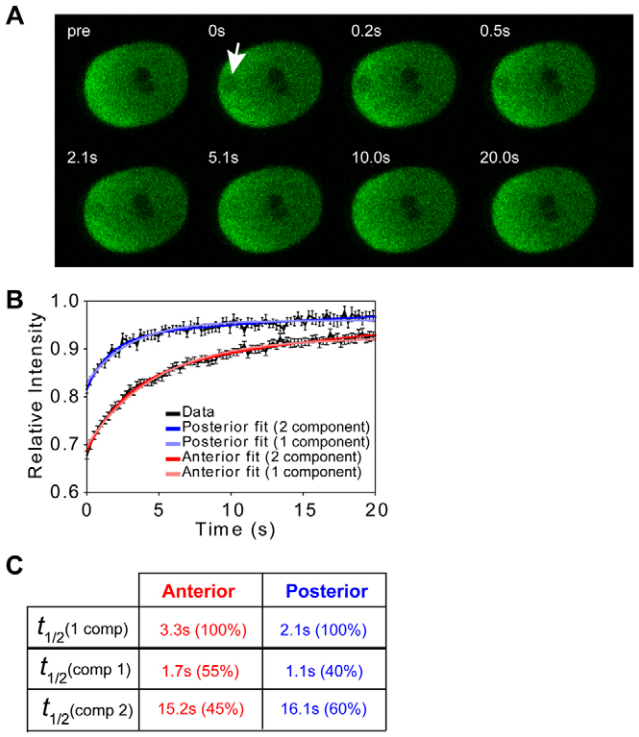


| | Anterior | Posterior |
|---|---|---|
| $t_{1/2}$(1 comp) | 3.3s (100%) | 2.1s (100%) |
| $t_{1/2}$(comp 1) | 1.7s (55%) | 1.1s (40%) |
| $t_{1/2}$(comp 2) | 15.2s (45%) | 16.1s (60%) |

**Fig. 1. Bulk dynamics of MEX-5::GFP in the *C. elegans* early embryo.** (**A**) Circular regions of interests (ROIs, arrow), 4.5 μm in diameter, were photobleached in either the anterior or posterior cytoplasm. (**B**) Fluorescence recovery curves were fitted to both one- and two-component diffusion curves for both anterior and posterior fluorescence recovery after photobleaching (FRAP). One-component recovery reveals overall asymmetry in the bulk diffusion rates of MEX-5::GFP. Improved data fitting by a multi-component model suggests the presence of multiple species of MEX-5::GFP, the diffusion coefficients of which differ by approximately an order of magnitude. (**C**) Theoretical diffusion curves can be broken down into individual components and reveal an asymmetry in the ratio of fast to slow MEX-5::GFP, with a higher ratio in the posterior cytoplasm. *C. elegans* zygotes are ~50 μm in length. s, seconds.

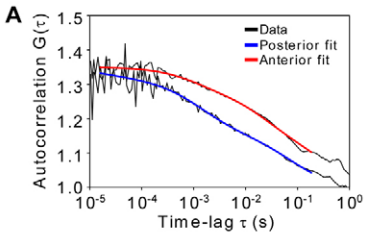


| | Anterior | Posterior |
|---|---|---|
| $D_M$ (μm²/s) | 17.5 ± 3.8 | 15.6 ± 4.3 |
| $D_{M^*}$ (μm²/s) | 0.6 ± 0.4 | 0.7 ± 0.3 |
| [M*]:[M] | 2.0 ± 0.1 | 0.9 ± 0.1 |

**Fig. 2. Fluorescence correlation spectroscopy (FCS) of MEX-5::GFP in the *C. elegans* early embryo.** (**A**) Normalized autocorrelation curves of FCS fluctuation data show differences between anterior and posterior diffusion of MEX-5::GFP. Statistical tests indicate the presence of multiple species of MEX-5::GFP in the cytoplasm ($P$<0.0001 for one-component model, F-test). (**B**,**C**) FCS theoretical diffusion curves predict species of MEX-5::GFP in the anterior cytoplasm with diffusion coefficients of 17.5±3.8 and 0.6±0.4 μm$^2$/second, and species of MEX-5::GFP in the posterior cytoplasm with diffusion coefficients of 15.6±4.3 and 0.7±0.3 μm$^2$/second. A third, slower component with a predicted diffusion coefficient of just 0.07±0.01 μm$^2$/second was also detected in both regions, suggesting an association with slow-moving granules. The ratio of slow to fast protein in the cytoplasm was determined to be 2.0±0.1 and 0.9±0.1 in the anterior and posterior, respectively. The slower bulk effective diffusion of MEX-5 in the anterior cytoplasm as measured by FRAP is presumably due to a higher proportion of slowly diffusing protein.

To further probe the behavior of diffusing MEX-5::GFP, we performed FCS analysis and fitted the resulting autocorrelation curves to one-, two- and three-component diffusion models. As expected, autocorrelation in the anterior region of the embryo decayed more slowly than on the posterior side, indicating slower bulk diffusion of MEX-5::GFP in the enriched anterior region of the embryo (Fig. 2A). F-distribution analysis strongly suggested the presence of multiple components throughout the cytoplasm of the embryo ($P$<0.0001 in both regions, F-test), as is expected for significant deviations from fits in underspecified models. FCS theoretical diffusion curves predicted that the diffusion coefficients of species of MEX-5::GFP were 17.5±3.8 and 0.6±0.4 μm$^2$/second in the anterior cytoplasm and 15.6±4.3 and 0.7±0.3 μm$^2$/second in the posterior cytoplasm (Fig. 2B,C). The ratios of slow to fast protein concentration were determined to be 2.0±0.1 and 0.9±0.1 in the anterior and posterior, respectively. The higher relative abundance of slowly diffusing protein in the anterior explains the overall slower bulk diffusion rates measured by FRAP. In each region, we also detected the presence of a component diffusing extremely slowly (0.07±0.01 μm$^2$/second), presumably as a result of the previously observed association of MEX-5::GFP with slow-moving granules (Tenlen et al., 2008). Based on our previous work, the presence of multiple protein species with substantially different diffusion coefficients in a system that exhibits a gradient in both bulk diffusion rates and fractional composition suggests a differential-diffusion model for MEX-5 enrichment (Daniels et al., 2009; Lipkow and Odde, 2008).

We next asked how well multi-component fitting of our experimental FRAP curves agrees with our FCS experiments. Fitting the curves to two-component recovery predicts species of MEX-5 with recovery half-times of 15.2 and 1.7 seconds in the anterior cytoplasm, and 16.1 and 1.1 seconds in the posterior cytoplasm (Fig. 1C). Thus, the recovery half-times of the two MEX-5 species in two-component FRAP differ by approximately an order of magnitude in both regions. Using a general equation for FRAP recovery (Soumpasis, 1983), we estimate the diffusion coefficients of the species of MEX-5 to be 0.3 and 2.6 μm$^2$/second and 0.3 and 4.1 μm$^2$/second in the anterior and posterior, respectively. Not surprisingly, these numbers underestimate the diffusion coefficients determined from FCS (more severely for the faster species) owing to the fact that significant diffusion takes place during the photobleaching step. Multi-component FRAP also

predicted relative ratios of the amount of slow to fast species of ~1:1 and ~2:3 in the anterior and posterior, respectively, consistent with the findings from FCS that the anterior cytoplasm contains a higher proportion of slowly diffusing MEX-5.

## Differential-diffusion model

In order to understand the mechanism by which MEX-5, a freely diffusing molecule, could be maintained in a gradient over large length scales and long time scales in *C. elegans* embryos, we sought to develop the simplest theoretical model possible that is consistent with all available data based on the differential-diffusion concept developed in our previous work (Daniels et al., 2009), recently published molecular evidence (Tenlen et al., 2008), and experimental data presented here. As a preliminary naïve model, we can begin by assuming that the enrichment of MEX-5 exists in both a rapidly diffusing form (*M*) and a slowly diffusing form (*M**) in the early embryo, as suggested by our experimental results. MEX-5 is converted heterogeneously from a slow to a fast form on a surface within the depleted side (posterior), presumably by phosphorylation by PAR-1, and is subsequently reverted to its slow form heterogeneously on a surface within the enriched side (anterior) of the embryo (Fig. 3A). After pronuclear meeting, the bulk levels of protein in the anterior and posterior cytoplasm remain constant for ~10 minutes (Tenlen et al., 2008), suggesting that the system evolves to a steady state. For a simplified one-dimensional system along the A/P axis of the zygote, this model predicts linear, constant-flux concentration profiles of each species across the zygote, which sum to a linear total concentration profile for MEX-5 (Fig. 3C).

This basic model correctly predicts an overall enrichment of MEX-5 in the anterior cytoplasm, but does not correctly predict the anterior enrichment of phospho-MEX-5 recently described (Tenlen et al., 2008). However, this discrepancy is easily remedied by including a third species of MEX-5 in our model (Fig. 3B). Specifically, rapidly diffusing, phosphorylated MEX-5, *A*, is converted heterogeneously to a slowly diffusing form of MEX-5, *B*, in the anterior, presumably by the PAR complex. This nascent species (*B*) is then dephosphorylated homogeneously, consistent with the presence of a uniformly distributed phosphatase in the cytoplasm. This unphosphorylated form, *C*, is then reverted back to *A* heterogeneously in the posterior by PAR-1 phosphorylation. Previous FRAP experiments have shown that the bulk diffusion rates of MEX-5 remain low in the mutant (S458A) that cannot be phosphorylated by PAR-1 (Tenlen et al., 2008). Previous FRAP experiments have shown that the bulk diffusion rates of MEX-5 remain low in the mutant (S458A) that cannot be phosphorylated by PAR-1 (Tenlen et al., 2008), suggesting that the diffusion coefficient of *C* must be low. Notably, the analytical solution of this system accurately predicts anterior enrichment of MEX-5 and phospho-MEX-5 (Fig. 3D) whether the diffusion coefficient of *C* is approximately equal to *A* or *B*. Moreover, this three-component differential-diffusion model with unique diffusion coefficients also allows for non-linear one-dimensional concentration profiles, as we observed experimentally (Fig. 4A,B). Thus, we propose a three-component, two-surface model to explain the anterior cytoplasmic enrichment of MEX-5, which predicts a steady-state one-dimensional overall concentration profile of:

$$\text{Total} = A_0 + C_0 + B_0\left(\frac{D_B}{D_C}\right) + \left(\frac{1}{D_A} - \frac{1}{D_C}\right) B_0 \sqrt{k_B D_B}\tanh\sqrt{\frac{k_B L^2}{D_B}}\,x + \left(1 - \frac{D_B}{D_C}\right) B_0 \frac{\cosh\left[\sqrt{\frac{k_B L^2}{D_B}}\left(1 - \frac{x}{L}\right)\right]}{\cosh\sqrt{\frac{k_B L^2}{D_B}}},$$

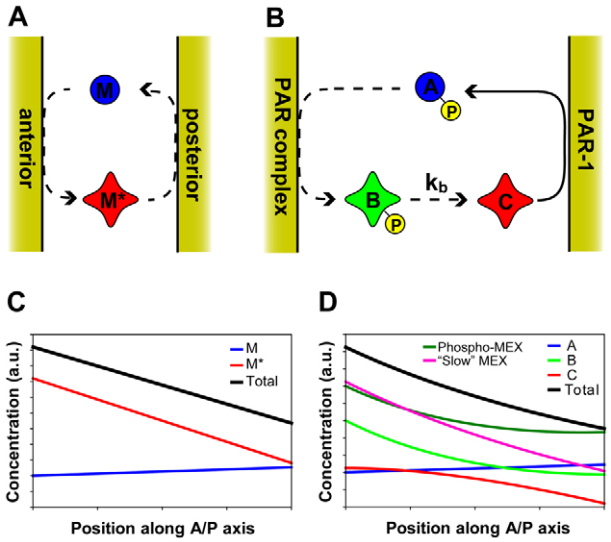


**Fig. 3. Differential-diffusion models for MEX-5 enrichment.** The differential-diffusion model proposed for MEX-5 enrichment involves two heterogeneous surface reactions. In the simple two-component case (**A**), one-dimensional analytical solutions yield linear concentration profiles for each species (**C**). We propose a three-component model that is consistent with all available data (**B**). Rapidly diffusing, phosphorylated MEX-5, *A*, is converted to a form with a decreased diffusion coefficient, *B*, by an anteriorly localized component (presumably the PAR complex, which consists of PAR-3, PAR-6 and PKC-3). This species is dephosphorylated homogeneously in the cytoplasm to generate an unphosphorylated species of MEX-5, *C*. Species *C* can then be rephosphorylated by posteriorly localized PAR-1 to regain its identity as *A* and complete the reaction cycle. This model qualitatively predicts the anterior enrichment of both MEX-5 and phosphorylated MEX-5 (phospho-MEX) (**D**). a.u., arbitrary units.

where $L$ is the length of the embryo along the spatial coordinate $x$, $A_0$, $B_0$ and $C_0$ are constants representing the relative concentrations of each species at the anterior surface ($x$=0), $D_A$, $D_B$ and $D_C$ are the diffusion coefficients of $A$, $B$ and $C$, respectively, and $k_B$ is the modified rate constant for the cytoplasmic $B \rightarrow C$ reaction.

It is worth noting that this system can be considered as diffusion limited, which is why the rate constants for the $C \rightarrow A$ and $A \rightarrow B$ reactions do not appear in the final equation; their values are implicit. For example, the rate constant for the $A \rightarrow B$ reaction, $k_A$, is found by considering the reaction rate at the anterior surface:

$$r_B = k_A A_0 = -D_B \left.\frac{dB}{dx}\right|_{x=0},$$

and thus:

$$k_A = -\frac{D_B}{A_0}\left.\frac{dB}{dx}\right|_{x=0}.$$

In this way, tuning of boundary concentrations is equivalent to tuning reaction constants. Furthermore, owing to the fact that the surface rate constants are also a function of the (unknown) surface concentration of catalyst, we are unable to obtain estimates of the physiological rate constants of these reactions. Similarly, the homogeneous rate constant $k_B$ is also assumed to be a function of the cytoplasmic concentration of phosphatase, which is also unknown (see Appendix S1 in the supplementary material).

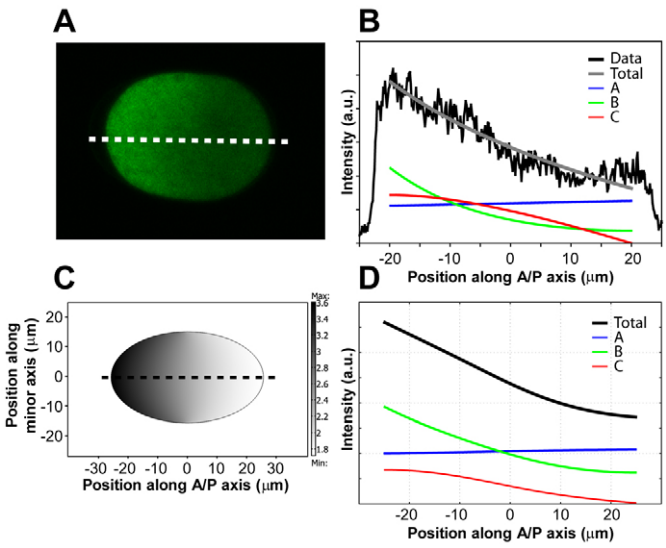


**Fig. 4. Experimental and theoretical concentration profiles.** Theoretical concentration profiles for MEX-5 obtained through one-dimensional analytical mathematical modeling and pseudo-three-dimensional computational modeling (axi-symmetric two-dimensional ovoid geometry with major and minor axis lengths of 50 μm and 30 μm, respectively) are compared with experimental fluorescence intensity profiles. A typical micrograph of a MEX-5::GFP embryo in the maintenance phase of polarization (**A**) and the corresponding fluorescence intensity profile across the A/P axis (dashed line), which agrees well with one-dimensional analytical predictions (**B**), as well as with computational pseudo-three-dimensional modeling (**C**,**D**).

We tested the ability of our model to correctly predict the observed concentration profile of MEX-5::GFP using intensity profiles obtained from fluorescence microscopy during mitosis. For the one-dimensional case, we assumed steady-state conditions, with the equal and opposite surface fluxes due to the reactions $A \rightarrow B$ and $C \rightarrow A$ at the anterior and posterior surfaces, respectively. In this time-invariant case, the concentration profiles of each species exist as stable gradients throughout the embryo. The analytical solution for the total concentration gradient predicted by this model was then fitted to experimental fluorescence intensity data and the fractional protein composition from FCS and was found to be well represented by our model (Fig. 4A,B). It should be noted that although PAR-1 is generally considered a posterior cortical protein, it is not strictly localized to the posterior cortex but is in fact also present in the cytoplasm (Guo and Kemphues, 1995). Since PAR-1 is assumed to act as the catalyst for the heterogeneous reaction, this discrepancy will have the effect of 'spreading' the posterior reaction, resulting in the 'plateau' in fluorescence observed in the posterior cytoplasm, which is unaccounted for in the model.

### Computational pseudo-three-dimensional model

In the above one-dimensional model, the forced flux at the reaction surfaces was assumed to be constant. However, in an actual embryo the reactant concentration may vary with position along the reaction surface, and therefore the rate of reaction might be expected to vary with position as well. In order to account for these geometric effects in our differential-diffusion model, we computationally modeled the system using COMSOL software (see Materials and methods and Appendix S1 in the supplementary material). Assuming that the zygote is axi-symmetrical about its long axis, we modeled the system as the central two-dimensional cross-section, the results of which will be independent of the angle of the cross-sectional plane. Based on light microscopy measurements, we approximated the zygote as an oval with major and minor axis lengths of 50 μm and 30 μm, respectively, centered about the origin with the anterior at $x<0$ and the posterior at $x>0$, and assigned diffusion coefficients to each species consistent with those obtained from FCS. We allowed the surface reactions to follow first-order kinetics: $A \rightarrow B$ proceeds at a rate of $k_A[A]$ on the system surface for $x<0$, and $C \rightarrow A$ proceeds at a rate of $k_C[C]$ on the system surface for $x>0$, with the $B \rightarrow C$ reaction taking place homogeneously (see Appendix S1 in the supplementary material). In all cases, species that are not involved in surface reactions are not allowed to diffuse through surfaces and are assigned zero flux values at boundaries: $B$ is not allowed to diffuse through the system boundary at the posterior, and $C$ is not allowed to diffuse through the system boundary at the anterior. As an arbitrary basis for calculation, we chose to set the value of $A$ at the anterior pole of the embryo as $A_0=1$ (arbitrary units). At steady state, we find that the two-dimensional system accurately predicts overall enrichment of MEX-5 in the anterior cytoplasm (Fig. 4), illustrating that the differential-diffusion model is applicable to three-dimensional systems and that various patterns may be attained by this robust differential-diffusion mechanism.

## DISCUSSION

Here, we propose a differential-diffusion model to explain the enrichment of MEX-5 in the *C. elegans* early embryo, as an alternative to the actomyosin binding model presented previously (Tenlen et al., 2008). The actomyosin binding model might have been inspired by the immobile fractions that were apparent in the recovery of MEX-5::GFP in their FRAP experiments, on average constituting 27% and 39% in the anterior and posterior, respectively (Tenlen et al., 2008). However, our FRAP measurements of MEX-5::GFP show substantially greater recovery, with immobile fractions ranging only as high as 8%, depending on the fitting model. Indeed, fitting the data to multi-component recovery yields an immobile fraction of 0%. We suspect that an experimental artifact is responsible for the reported apparent immobile fractions (Tenlen et al., 2008), considering that the authors also found a significant immobile fraction of 68% for free GFP in the embryos, which would be expected to be freely mobile. We found an immobile fraction of 0% for GFP alone (our unpublished data).

The enrichment of proteins (i.e. PIE-1, POS-1) in the posterior cytoplasm cannot be explained by the binding of proteins to an anteriorly localized actomyosin network. Assuming that the actomyosin network does in fact play a role in the enrichment of PIE-1 and MEX-5, a simple way to reconcile these two models would involve localized modulation of the binding of each of these proteins to a uniform cytoskeletal network. Physically, this is equivalent to changing the heterogeneous reactions from 'fast → slow' to 'low-affinity binding → high-affinity binding' forms of the proteins. The affinity of bound proteins may then be reversed by interaction with a homogeneous component, which would be expected to follow first-order reversion, and the resultant analytical profiles should be equivalent. The low-affinity (unbound) form of each protein will have a large diffusion coefficient, whereas the high-affinity (bound) form of the protein will have a small diffusion coefficient. The key distinction in this case is that this model does not require asymmetric binding sites, in contrast to the actomyosin binding model (Tenlen et al., 2008). As such, the role of PAR-1

might be to decrease the binding affinity of MEX-5 to a putative component, and the previously unassigned role of PAR-4 might be to increase this binding affinity or to stabilize the complex.

It has been shown that ectopically localized *par-1* mutants (*b274*, *e2012*, *it60*) with kinase activity are not able to correctly segregate MEX-5 to the anterior (Tenlen et al., 2008). Because these *par-1* mutants are able to phosphorylate MEX-5 at S458 yet are partitioning defective, it has been suggested that *par-1* might have some additional role in the process distinct from S458 phosphorylation (Tenlen et al., 2008). The results of our model provide an explanation for this finding. The mislocalization of active PAR-1 from the posterior cortex to the bulk cytoplasm will result in conversion of MEX-5 from the slow to the fast form in the anterior cytoplasm, greatly reducing gross A/P asymmetry. Furthermore, it might also be possible that PAR-1 can act directly on species *B* as well as *C*, thus causing an even more severe abrogation of MEX-5 enrichment in embryos containing mislocalized PAR-1. Therefore, it is not surprising that we see no sign of MEX-5 enrichment in *par-1(b274)* embryos, despite the fact that MEX-5 is still phosphorylated by PAR-1. Physically, PAR-1 may have the ability to phosphorylate MEX-5 at multiple sites (distinct from S458). This variation of our model, in which species *B* is allowed to attain a positive flux at the posterior surface ($x=L$), predicts an overall concentration profile of:

$$\begin{aligned}\text{Total} &= A + B + C \\ &= A_0 + C_0 + \frac{D_B}{D_C}B_0 + \left(1-\frac{D_B}{D_C}\right)B_0 \exp\left(-\sqrt{\frac{k_B}{D_B}}x\right) \\ &+ \left(1-\frac{D_B}{D_C}\right)\frac{\left[B_0\sqrt{k_B D_B}\exp\left(-\sqrt{\frac{k_B}{D_B}}L\right)-\beta\right]\left[\exp\left(\sqrt{\frac{k_B}{D_B}}x\right)-\exp\left(-\sqrt{\frac{k_B}{D_B}}x\right)\right]}{\sqrt{k_B D_B}\left[\exp\left(\sqrt{\frac{k_B}{D_B}}L\right)+\exp\left(-\sqrt{\frac{k_B}{D_B}}L\right)\right]} \\ &+ \left(\frac{1}{D_A}-\frac{1}{D_C}\right)\left\{2\frac{\left[\beta - B_0\sqrt{k_B D_B}\exp\left(-\sqrt{\frac{k_B}{D_B}}L\right)\right]}{\left[\exp\left(\sqrt{\frac{k_B}{D_B}}L\right)+\exp\left(-\sqrt{\frac{k_B}{D_B}}L\right)\right]}+\sqrt{k_B D_B}B_0\right\}x\,,\end{aligned}$$

in wild-type embryos, where β is the effective flux of species *B* at $x=L$. This prediction is very similar to that of our general model in wild-type embryos (see Appendix S1 in the supplementary material), but may more thoroughly explain the complete loss of MEX-5 enrichment in the *par-1(b274)* mutants.

Importantly, the MEX-5 enrichment model presented here may also represent an alternative model to the current PIE-1 enrichment model (Daniels et al., 2009). For example, our previous speculation that the diffusion coefficient might be decreased by binding a nucleic acid may be broadened to include cytoskeletal components as well. Furthermore, it might be that the role of MEX-5/6 in PIE-1 enrichment is to mediate the conversion between slowly and rapidly diffusing forms of PIE-1, or even a hypothetical conversion between putative unequally phosphorylated 'heavy' forms of PIE-1, similar to those of MEX-5 proposed here (species *B* and *C*).

We demonstrate that a differential-diffusion model is consistent with all available data for MEX-5 enrichment and might in fact be the only thoroughly consistent model to date. As such, we extend the scope of these reaction/diffusion models to include not only germline morphogens, but also somatic determinants. Considering that this trend is emerging as a primary mechanism of protein enrichment in the nematode *C. elegans* and given its intimate link to the highly conserved PAR proteins, we anticipate that similar reaction/diffusion mechanisms operate within a variety of metazoan cell types. Interestingly, it was recently reported that in the syncytial blastoderm of *Drosophila melanogaster*, an asymmetrically localized cortical receptor complex (Toll) mediates the asymmetric localization of the transcription factor Dorsal by altering, through phosphorylation, its ability to form a complex (DeLotto et al., 2007; Kanodia et al., 2009; Shvartsman et al., 2008). In this case, Dorsal is unable to enter nuclei when associated with its binding partner (Cactus), but gains the ability to enter nuclei once dissociation of its complex is triggered by the ventrally localized, activated Toll receptor. Thus, the cortical signal drives differential cytoplasmic gradients of free Dorsal and the Dorsal-Cactus complex, resulting in elevated levels of Dorsal in ventral nuclei. However, in contrast to our model, the enrichment of Dorsal is not due to a change in its diffusion coefficient resulting from phosphorylation, but rather to a change in its ability to shuttle into nuclei (which constitute a significant fraction of the accessible volume of Dorsal). Alternatively, nuclear Dorsal may be thought of as part of a 'Dorsal-nuclear' complex with an effective diffusion coefficient of zero, in which case the dissociation of the Dorsal-Cactus complex actually leads to a decrease in the rate of diffusion of Dorsal. Consequently, in this system, Dorsal becomes enriched in the vicinity of the phosphorylating signal, in contrast to the situation in the *C. elegans* early embryo, in which MEX-5 is depleted in the vicinity of the phosphorylating signal. Therefore, it appears that unique variations on the class of reaction/diffusion mechanism presented here might operate within a variety of metazoan cell types.

**Acknowledgements**

We thank Geraldine Seydoux for reagents; Mark van Doren, Cathy Royer, David Wolf, Timothy Daniels, Jennifer Lippincott-Schwartz and Hongyuan Jiang for helpful discussions and technical advice; and Michelle Husain, Forbes McCaffery and Michael McCaffery for help with microscopy. We acknowledge support from the NIH (GM075305 and CA143868). Deposited in PMC for release after 12 months.

**Competing interests statement**

The authors declare no competing financial interests.

**Supplementary material**

Supplementary material for this article is available at http://dev.biologists.org/lookup/suppl/doi:10.1242/dev.051326/-/DC1

**References**

**Betschinger, J. and Knoblich, J. A.** (2004). Dare to be different: asymmetric cell division in *Drosophila*, *C. elegans* and vertebrates. *Curr. Biol.* **14**, R674-R685.
**Brenner, S.** (1974). The genetics of Caenorhabditis elegans. *Genetics* **77**, 71-94.
**Crick, F.** (1970). Diffusion in embryogenesis. *Nature* **225**, 420-422.
**Cuenca, A. A., Schetter, A., Aceto, D., Kemphues, K. and Seydoux, G.** (2003). Polarization of the C. elegans zygote proceeds via distinct establishment and maintenance phases. *Development* **130**, 1255-1265.
**Daniels, B. R., Masi, B. C. and Wirtz, D.** (2006). Probing single-cell micromechanics in vivo: the microrheology of C. elegans developing embryos. *Biophys. J.* **90**, 4712-4719.
**Daniels, B. R., Perkins, E. M., Dobrowsky, T. M., Sun, S. X. and Wirtz, D.** (2009). Asymmetric enrichment of PIE-1 in the Caenorhabditis elegans zygote mediated by binary counterdiffusion. *J. Cell Biol.* **184**, 473-479.
**DeLotto, R., DeLotto, Y., Steward, R. and Lippincott-Schwartz, J.** (2007). Nucleocytoplasmic shuttling mediates the dynamic maintenance of nuclear Dorsal levels during Drosophila embryogenesis. *Development* **134**, 4233-4241.
**Gregor, T., Wieschaus, E. F., McGregor, A. P., Bialek, W. and Tank, D. W.** (2007). Stability and nuclear dynamics of the bicoid morphogen gradient. *Cell* **130**, 141-152.
**Grill, S. W., Gonczy, P., Stelzer, E. H. and Hyman, A. A.** (2001). Polarity controls forces governing asymmetric spindle positioning in the Caenorhabditis elegans embryo. *Nature* **409**, 630-633.
**Guo, S. and Kemphues, K. J.** (1995). par-1, a gene required for establishing polarity in C. elegans embryos, encodes a putative Ser/Thr kinase that is asymmetrically distributed. *Cell* **81**, 611-620.

**Kanodia, J. S., Rikhy, R., Kim, Y., Lund, V. K., DeLotto, R., Lippincott-Schwartz, J. and Shvartsman, S. Y.** (2009). Dynamics of the Dorsal morphogen gradient. *Proc. Natl. Acad. Sci. USA* **106**, 21707-21712.
**Lipkow, K. and Odde, D. J.** (2008). Model for protein concentration gradients in the cytoplasm. *Cell. Mol. Bioeng.* **1**, 84-92.
**Reddy, J. N.** (1993). *An Introduction to the Finite Element Method*, 4th edn. London: McGraw-Hill.
**Shvartsman, S. Y., Coppey, M. and Berezhkovskii, A. M.** (2008). Dynamics of maternal morphogen gradients in Drosophila. *Curr. Opin. Genet. Dev.* **18**, 342-347.
**Soumpasis, D. M.** (1983). Theoretical analysis of fluorescence photobleaching recovery experiments. *Biophys. J.* **41**, 95-97.
**Sun, S. X., Farrell, B., Chana, M. S., Oster, G., Brownell, W. E. and Spector, A. A.** (2009). Voltage and frequency dependence of prestin-associated charge transfer. *J. Theor. Biol.* **260**, 137-144.
**Tenlen, J. R., Molk, J. N., London, N., Page, B. D. and Priess, J. R.** (2008). MEX-5 asymmetry in one-cell C. elegans embryos requires PAR-4- and PAR-1-dependent phosphorylation. *Development* **135**, 3665-3675.
**Tostevin, F. and Howard, M.** (2008). Modeling the establishment of PAR protein polarity in the one-cell C. elegans embryo. *Biophys. J.* **95**, 4512-4522.

**SUPPLEMENTAL MATERIAL**

**Derivation of 1D analytical concentration profiles**

Steady-state post-enrichment, 1D model

The steady-state equations of change for diffusing species *A*, *B*, and *C* are:

$$\frac{\partial A}{\partial t} = 0 = D_A \frac{\partial^2 A}{\partial x^2} \tag{1}$$

$$\frac{\partial B}{\partial t} = 0 = D_B \frac{\partial^2 B}{\partial x^2} - k_B B \tag{2}$$

$$\frac{\partial C}{\partial t} = 0 = D_C \frac{\partial^2 C}{\partial x^2} + k_B B \tag{3}$$

The boundary conditions are:

$$J_A\big|_0 = J_A\big|_L = J \tag{4}$$

$$J_B\big|_0 = -J_A\big|_0 = J \tag{5}$$

$$J_B\big|_L = 0 \tag{6}$$

$$J_C\big|_0 = 0 \tag{7}$$

$$J_C\big|_L = -J_A\big|_0 = J \tag{8}$$

where *J* is the flux. These conditions state that the flux from the reaction surfaces are diffusion-limited (hence they do not contain rate constants and do not depend on reactant concentration) and constant at steady-state. As a basis of calculation, we allow the surface reaction of *B*, *B*(0), to reach an arbitrary constant value of $B_0$ at steady-state, which will ultimately depend on system parameters such as the reaction rate constants and total amount of protein present in the embryo (see below).

Solving for $A$:

$$\frac{\partial^2 A}{\partial x^2} = 0$$

$$\frac{\partial A}{\partial x} = m$$

$$A = mx + A_0 \tag{9}$$

where $A_0$ is the concentration of $A$ at $x$=0. We see that $A$ is linear, and the flux of $A$ is constant over all $x$ from 0 to L.

$$J_A = -D_A \frac{dA}{dx} = -D_A m$$

Solving for $B$:

$$\frac{\partial^2 B}{\partial x^2} = \frac{k_B}{D_B} B$$

With steady flux at $x$=0 and zero flux at $x$=L, we expect the concentration of $B$ to achieve an arbitrary steady value we will denote by the constant $B_0$, such that

$$B = B_0 \frac{\cosh\left[\sqrt{\frac{k_B L^2}{D_B}}\left(1 - \frac{x}{L}\right)\right]}{\cosh\sqrt{\frac{k_B L^2}{D_B}}} \tag{10}$$

We see that the flux of $B$ is

$$J_B = -D_B \frac{dB}{dx} = B_0 \sqrt{k_B D_B} \frac{\sinh\left[\sqrt{\frac{k_B L^2}{D_B}}\left(1 - \frac{x}{L}\right)\right]}{\cosh\sqrt{\frac{k_B L^2}{D_B}}}$$

so the flux of *B* at 0 is

$$J_B\big|_0 = B_0\sqrt{k_B D_B}\,\frac{\sinh\sqrt{\frac{k_B L^2}{D_B}}}{\cosh\sqrt{\frac{k_B L^2}{D_B}}} = B_0\sqrt{k_B D_B}\,\tanh\sqrt{\frac{k_B L^2}{D_B}}$$

and the flux of *B* at L is

$$J_B\big|_L = B_0\sqrt{k_B D_B}\,\frac{\sinh(0)}{\cosh\sqrt{\frac{k_B L^2}{D_B}}} = 0$$

Solving for *C*:

$$\frac{\partial^2 C}{\partial x^2} = -\frac{k_B}{D_B}B = -\frac{k_B}{D_B}B_0\,\frac{\cosh\left[\sqrt{\frac{k_B L^2}{D_B}}\left(1-\frac{x}{L}\right)\right]}{\cosh\sqrt{\frac{k_B L^2}{D_B}}}$$

$$\frac{\partial C}{\partial x} = \frac{B_0}{D_C}\sqrt{D_B k_B}\,\frac{\sinh\left[\sqrt{\frac{k_B L^2}{D_B}}\left(1-\frac{x}{L}\right)\right]}{\cosh\sqrt{\frac{k_B L^2}{D_B}}} + c_1$$

$$C = -B_0\left(\frac{D_B}{D_C}\right)\frac{\cosh\left[\sqrt{\frac{k_B L^2}{D_B}}\left(1-\frac{x}{L}\right)\right]}{\cosh\sqrt{\frac{k_B L^2}{D_B}}} + c_1 x + c_2$$

We can solve for $c_1$ by considering the zero flux condition at $x$=0:

$$J_C\big|_0 = 0 = -D_C\left.\frac{\partial C}{\partial x}\right|_0$$

$$\left.\frac{\partial C}{\partial x}\right|_0 = 0 = \frac{B_0}{D_C}\sqrt{D_B k_B}\tanh\sqrt{\frac{k_B L^2}{D_B}} + c_1$$

$$c_1 = -\frac{B_0}{D_C}\sqrt{D_B k_B}\tanh\sqrt{\frac{k_B L^2}{D_B}}$$

Plugging in for $c_1$, we obtain

$$C = -B_0\left(\frac{D_B}{D_C}\right)\frac{\cosh\left[\sqrt{\frac{k_B L^2}{D_B}}\left(1-\frac{x}{L}\right)\right]}{\cosh\sqrt{\frac{k_B L^2}{D_B}}} - \frac{B_0}{D_C}\sqrt{D_B k_B}\tanh\sqrt{\frac{k_B L^2}{D_B}}x + c_2$$

The flux of $C$ is

$$\frac{\partial C}{\partial x} = \frac{B_0}{D_C}\sqrt{D_B k_B}\frac{\sinh\left[\sqrt{\frac{k_B L^2}{D_B}}\left(1-\frac{x}{L}\right)\right]}{\cosh\sqrt{\frac{k_B L^2}{D_B}}} - \frac{B_0}{D_C}\sqrt{D_B k_B}\tanh\sqrt{\frac{k_B L^2}{D_B}}$$

Similarly to the case for $B$, with a steady flux of $C$ at $x$=L, we expect the concentration of $C$ to attain a steady value at $x$=0 that we will denote $C_0$, such that

$$C(0) = C_0 = -B_0\left(\frac{D_B}{D_C}\right) + c_2$$

$$C_2 = C_0 + B_0\left(\frac{D_B}{D_C}\right)$$

Plugging in for $c_2$, we obtain

$$C = C_0 + B_0\left(\frac{D_B}{D_C}\right)\left[1 - \frac{\cosh\left[\sqrt{\frac{k_B L^2}{D_B}}\left(1-\frac{x}{L}\right)\right]}{\cosh\sqrt{\frac{k_B L^2}{D_B}}}\right] - \frac{B_0}{D_C}\sqrt{k_B D_B}\tanh\sqrt{\frac{k_B L^2}{D_B}}x$$

(11)

The flux of $C$ is

$$J_C = -D_C \frac{\partial C}{\partial x} = -B_0 \sqrt{D_B k_B} \frac{\sinh\left[\sqrt{\frac{k_B L^2}{D_B}}\left(1-\frac{x}{L}\right)\right]}{\cosh\sqrt{\frac{k_B L^2}{D_B}}} + B_0 \sqrt{D_B k_B} \tanh\sqrt{\frac{k_B L^2}{D_B}}$$

So the flux at $x$=0 is

$$J_C\big|_0 = -D_C \left.\frac{\partial C}{\partial x}\right|_0 = -B_0 \sqrt{D_B k_B} \tanh\sqrt{\frac{k_B L^2}{D_B}} + B_0 \sqrt{D_B k_B} \tanh\sqrt{\frac{k_B L^2}{D_B}} = 0$$

And the flux at $x$=L is

$$J_C\big|_L = -D_C \left.\frac{\partial C}{\partial x}\right|_L = B_0 \sqrt{D_B k_B} \tanh\sqrt{\frac{k_B L^2}{D_B}}$$

which, as expected, is equal to the flux of $B$ at $x$=0. Of course, the flux of $B$ at $x$=0 must be equal and opposite of the flux of $A$ at $x$=0. Likewise, the flux of $C$ at $x$=L must be equal and opposite to the flux of $A$ at $x$=L. Hence,

$$J_B\big|_0 = B_0 \sqrt{k_B D_B} \tanh\sqrt{\frac{k_B L^2}{D_B}} = -J_A\big|_0 = D_A m$$

So

$$m = \frac{B_0}{D_A} \sqrt{k_B D_B} \tanh\sqrt{\frac{k_B L^2}{D_B}}$$

We can check the flux at x=L…

$$J_C\big|_L = B_0 \sqrt{D_B k_B} \tanh\sqrt{\frac{k_B L^2}{D_B}} = J_A\big|_L = D_A m$$

And we again find that

$$m = \frac{B_0}{D_A}\sqrt{D_B k_B}\,\tanh\sqrt{\frac{k_B L^2}{D_B}}$$

Hence,

$$A = mx + A_0 = \left(\frac{B_0}{D_A}\sqrt{D_B k_B}\,\tanh\sqrt{\frac{k_B L^2}{D_B}}\right)x + A_0 \qquad (13)$$

$A_0$, which determines the relative concentration of $A$ in the system, is left as a tunable parameter.

The total concentration can then be calculated by

$$Total = A + B + C$$

$$Total = A_0 + C_0 + B_0\left(\frac{D_B}{D_C}\right) + \left(\frac{1}{D_A} - \frac{1}{D_C}\right)B_0\sqrt{k_B D_B}\,\tanh\sqrt{\frac{k_B L^2}{D_B}}x + \left(1 - \frac{D_B}{D_C}\right)B_0\frac{\cosh\left[\sqrt{\frac{k_B L^2}{D_B}}\left(1 - \frac{x}{L}\right)\right]}{\cosh\sqrt{\frac{k_B L^2}{D_B}}} \qquad (14)$$

In order to test the ability of our model to correctly predict the overall concentration gradient, we measured fluorescence intensity along the A/P axis of embryos expressing MEX-5::GFP (with background fluorescence subtracted) and used data from the central 40um of the A/P axis ($L$), and used values for the diffusion coefficients ($D_A$, $D_B$, $D_C$) measured with FCS. Species intensity ($A_0$, $B_0$, $C_0$) and reaction ($k_B$) parameters were tuned to minimize squared error. Diffusion coefficients for slow system components ($B$ and $C$) were constants equal to 0.4 $\mu m^2/s$ and 1.0 $\mu m^2/s$, respectively, while the diffusion coefficient for the fast species ($A$) was constant and equal to 15 $\mu m^2/s$ (all of which are within experimental error of our FCS measurements). As

a basis for calculation, the total intensity at the anterior pole ($x$=0μm) was normalized to $Total(0)$ = 5 (a.u.).

The rate constants used in our modeling are modified such that $k_{cytoplasmic} = k_{phys} k_I [P]$ and $k_{surface} = k_{phys} k_I \frac{E_{tot}}{K_M}$ (assuming first order surface reactions), where $k_{phys}$ is the physiological rate constant, $k_I = \frac{[S]}{S}$ is an (unknown) constant relating fluorescence intensity (S) to cytoplasmic concentration ([S]), [$P$] is the (unknown) concentration of the putative cytoplasmic phosphatase, $E_{tot}$ is the (unknown) total surface concentration of enzyme on the reaction surface, $K_M$ is the Michaelis constant, and $k_{phys}$ is the physiological rate constant. The modified rate constants estimated from the modeling were $k_A$=0.065 μm/s, $k_B$ = 0.0025 $s^{-1}$, and $k_C$ = 0.2 μm/s, and the concentration parameters (a.u.) were estimated to be $A_0$ = 1, $B_0$ = 2.1, $C_0$ = 1.9.

**FEMLAB**

Multi-dimensional solutions to the partial differential equations were found using the finite element method (FEM) via COMSOL 3.5a (FEMLAB) software. FEM analysis is a useful tool for calculating solutions to complicated systems of equations over complex geometries including intricate biological problems (Reddy, 1993; Sun et al., 2009). Briefly, the finite element method calculates the solution to complicated systems by breaking the geometry of a given system into subdomains, or finite elements. Solutions to each finite element are calculated by approximating solutions to the partial differential equations over that element as a linear sum of algebraic polynomials where the undetermined coefficients of these polynomials are valued according to the governing partial differential equations. The finite elements themselves are not fixed throughout solving the governing system of equations but may change to reduce the error

in approximation over a given element and maintain continuity of the solution over all elements (Reddy, 1993).

Here, we used a simple oval geometry (major and minor axes of 50μm and 30μm, respectively) centered about the origin, consisting of two spatially identical and opposite reactive surfaces, the anterior and posterior, to represent the dividing embryo. The *A* to *B* reactions were allowed to occur only on the anterior surface, the *B* to *C* reaction again occurred everywhere within the cytoplasmic region and the *C* to *A* reaction was allowed to occur only on the posterior surface. All reactions rates used to calculate the multi-dimensional solutions were first order. Diffusion coefficients for slow system components (*B* and *C*) were constants equal to 0.4 $\mu m^2/s$ and 1.0 $\mu m^2/s$, respectively, while the diffusion coefficient for the fast species (*A*) was constant and equal to 15 $\mu m^2/s$ (all of which are within experimental error of our FCS measurements). As a basis for calculation, the concentration of *A* at the anterior pole (far left anterior node) was considered a known quantity and set equal to 1 (a.u.). The modified rate constants (see above) used in the modeling were $k_A$=0.02 μm/s, $k_B$ = 0.001 $s^{-1}$ and $k_C$ = 0.5 μm/s.

**Analytical concentration profiles with reactive species *B***

The governing equations are identical to those for the non-reacting *B* species, however the zero-flux boundary condition at $x = L$ must be allowed to take some finite value, $\beta$. Thus, the general equation for species *B* becomes

$$B = a\exp\left(\sqrt{\frac{k_B}{D_B}}x\right) + b\exp\left(-\sqrt{\frac{k_B}{D_B}}x\right)$$

We specify that *B* attains for steady-state value at $x=0$ such that

$$B(0) = B_0 = a + b$$

$$b = B_0 - a$$

$$B = a\exp\left(\sqrt{\frac{k_B}{D_B}}x\right) + (B_0 - a)\exp\left(-\sqrt{\frac{k_B}{D_B}}x\right)$$

$$B = a\exp\left(\sqrt{\frac{k_B}{D_B}}x\right) - a\exp\left(-\sqrt{\frac{k_B}{D_B}}x\right) + B_0\exp\left(-\sqrt{\frac{k_B}{D_B}}x\right)$$

$$B = a\left[\exp\left(\sqrt{\frac{k_B}{D_B}}x\right) - \exp\left(-\sqrt{\frac{k_B}{D_B}}x\right)\right] + B_0\exp\left(-\sqrt{\frac{k_B}{D_B}}x\right)$$

and

$$\frac{dB}{dx} = \sqrt{\frac{k_B}{D_B}}a\exp\left(\sqrt{\frac{k_B}{D_B}}x\right) - \sqrt{\frac{k_B}{D_B}}(B_0 - a)\exp\left(-\sqrt{\frac{k_B}{D_B}}x\right)$$

$$\frac{dB}{dx} = \sqrt{\frac{k_B}{D_B}}a\exp\left(\sqrt{\frac{k_B}{D_B}}x\right) + \sqrt{\frac{k_B}{D_B}}a\exp\left(-\sqrt{\frac{k_B}{D_B}}x\right) - \sqrt{\frac{k_B}{D_B}}B_0\exp\left(-\sqrt{\frac{k_B}{D_B}}x\right)$$

$$\frac{dB}{dx} = a\sqrt{\frac{k_B}{D_B}}\left[\exp\left(\sqrt{\frac{k_B}{D_B}}x\right) + \exp\left(-\sqrt{\frac{k_B}{D_B}}x\right)\right] - \sqrt{\frac{k_B}{D_B}}B_0\exp\left(-\sqrt{\frac{k_B}{D_B}}x\right)$$

We allow the flux of *B* to attain some finite value, $\beta$, at steady-state such that

$$J_B = -D_B \left.\frac{dB}{dx}\right|_{x=L} = \beta = -\sqrt{k_B D_B}\, a \exp\left(\sqrt{\frac{k_B}{D_B}} L\right) + \sqrt{k_B D_B}\,(B_0 - a)\exp\left(-\sqrt{\frac{k_B}{D_B}} L\right)$$

$$\beta = B_0 \sqrt{k_B D_B}\, \exp\left(-\sqrt{\frac{k_B}{D_B}} L\right) - a\sqrt{k_B D_B}\, \exp\left(-\sqrt{\frac{k_B}{D_B}} L\right) - a\sqrt{k_B D_B}\, \exp\left(\sqrt{\frac{k_B}{D_B}} L\right)$$

$$\beta = B_0 \sqrt{k_B D_B}\, \exp\left(-\sqrt{\frac{k_B}{D_B}} L\right) - a\sqrt{k_B D_B}\left[\exp\left(\sqrt{\frac{k_B}{D_B}} L\right) + \exp\left(-\sqrt{\frac{k_B}{D_B}} L\right)\right]$$

$$a = \frac{B_0 \sqrt{k_B D_B}\, \exp\left(-\sqrt{\frac{k_B}{D_B}} L\right) - \beta}{\sqrt{k_B D_B}\left[\exp\left(\sqrt{\frac{k_B}{D_B}} L\right) + \exp\left(-\sqrt{\frac{k_B}{D_B}} L\right)\right]}$$

$$B = \frac{\left[B_0 \sqrt{k_B D_B}\, \exp\left(-\sqrt{\frac{k_B}{D_B}} L\right) - \beta\right]}{\sqrt{k_B D_B}} \frac{\left[\exp\left(\sqrt{\frac{k_B}{D_B}} x\right) - \exp\left(-\sqrt{\frac{k_B}{D_B}} x\right)\right]}{\left[\exp\left(\sqrt{\frac{k_B}{D_B}} L\right) + \exp\left(-\sqrt{\frac{k_B}{D_B}} L\right)\right]} + B_0 \exp\left(-\sqrt{\frac{k_B}{D_B}} x\right)$$

$$\frac{dB}{dx} = \frac{\left[B_0 \sqrt{k_B D_B}\, \exp\left(-\sqrt{\frac{k_B}{D_B}} L\right) - \beta\right]}{D_B} \frac{\left[\exp\left(\sqrt{\frac{k_B}{D_B}} x\right) + \exp\left(-\sqrt{\frac{k_B}{D_B}} x\right)\right]}{\left[\exp\left(\sqrt{\frac{k_B}{D_B}} L\right) + \exp\left(-\sqrt{\frac{k_B}{D_B}} L\right)\right]} - \sqrt{\frac{k_B}{D_B}} B_0 \exp\left(-\sqrt{\frac{k_B}{D_B}} x\right)$$

where $\beta$ is a constant. Thus, the flux of B is given by

$$J_B = -D_B \frac{dB}{dx} = \left[\beta - B_0 \sqrt{k_B D_B}\, \exp\left(-\sqrt{\frac{k_B}{D_B}} L\right)\right] \frac{\left[\exp\left(\sqrt{\frac{k_B}{D_B}} x\right) + \exp\left(-\sqrt{\frac{k_B}{D_B}} x\right)\right]}{\left[\exp\left(\sqrt{\frac{k_B}{D_B}} L\right) + \exp\left(-\sqrt{\frac{k_B}{D_B}} L\right)\right]} + \sqrt{k_B D_B}\, B_0 \exp\left(-\sqrt{\frac{k_B}{D_B}} x\right)$$

We can use the explicit expression for $B$ to solve for $C$ by integration

$$\frac{d^2C}{dx^2} = -\frac{k_B}{D_C}B = -\frac{k_B}{D_C}\frac{\left[B_0\sqrt{k_B D_B}\exp\left(-\sqrt{\frac{k_B}{D_B}}L\right)-\beta\right]}{\sqrt{k_B D_B}}\frac{\left[\exp\left(\sqrt{\frac{k_B}{D_B}}x\right)-\exp\left(-\sqrt{\frac{k_B}{D_B}}x\right)\right]}{\left[\exp\left(\sqrt{\frac{k_B}{D_B}}L\right)+\exp\left(-\sqrt{\frac{k_B}{D_B}}L\right)\right]} - \frac{k_B}{D_C}B_0\exp\left(-\sqrt{\frac{k_B}{D_B}}x\right)$$

$$\frac{dC}{dx} = -\frac{\left[B_0\sqrt{k_B D_B}\exp\left(-\sqrt{\frac{k_B}{D_B}}L\right)-\beta\right]}{D_C}\frac{\left[\exp\left(\sqrt{\frac{k_B}{D_B}}x\right)+\exp\left(-\sqrt{\frac{k_B}{D_B}}x\right)\right]}{\left[\exp\left(\sqrt{\frac{k_B}{D_B}}L\right)+\exp\left(-\sqrt{\frac{k_B}{D_B}}L\right)\right]} + \frac{\sqrt{k_B D_B}}{D_C}B_0\exp\left(-\sqrt{\frac{k_B}{D_B}}x\right) + c_1$$

The flux of $C$ at $x$=0 is specified to equal 0 such that

$$\left.\frac{dC}{dx}\right|_{x=0} = 0 = -\frac{\left[B_0\sqrt{k_B D_B}\exp\left(-\sqrt{\frac{k_B}{D_B}}L\right)-\beta\right]}{\left[\exp\left(\sqrt{\frac{k_B}{D_B}}L\right)+\exp\left(-\sqrt{\frac{k_B}{D_B}}L\right)\right]}\frac{2}{D_C} + \frac{\sqrt{k_B D_B}}{D_C}B_0 + c_1$$

$$c_1 = \frac{\left[B_0\sqrt{k_B D_B}\exp\left(-\sqrt{\frac{k_B}{D_B}}L\right)-\beta\right]}{\left[\exp\left(\sqrt{\frac{k_B}{D_B}}L\right)+\exp\left(-\sqrt{\frac{k_B}{D_B}}L\right)\right]}\frac{2}{D_C} - \frac{\sqrt{k_B D_B}}{D_C}B_0$$

$$\frac{dC}{dx} = -\frac{\left[B_0\sqrt{k_B D_B}\exp\left(-\sqrt{\frac{k_B}{D_B}}L\right)-\beta\right]}{D_C}\frac{\left[\exp\left(\sqrt{\frac{k_B}{D_B}}x\right)+\exp\left(-\sqrt{\frac{k_B}{D_B}}x\right)\right]}{\left[\exp\left(\sqrt{\frac{k_B}{D_B}}L\right)+\exp\left(-\sqrt{\frac{k_B}{D_B}}L\right)\right]} + \frac{\sqrt{k_B D_B}}{D_C}B_0\exp\left(-\sqrt{\frac{k_B}{D_B}}x\right)$$
$$+\frac{\left[B_0\sqrt{k_B D_B}\exp\left(-\sqrt{\frac{k_B}{D_B}}L\right)-\beta\right]}{\left[\exp\left(\sqrt{\frac{k_B}{D_B}}L\right)+\exp\left(-\sqrt{\frac{k_B}{D_B}}L\right)\right]}\frac{2}{D_C} - \frac{\sqrt{k_B D_B}}{D_C}B_0$$

$$C = c_2 - \sqrt{\frac{D_B}{k_B}} \frac{\left[ B_0 \sqrt{k_B D_B} \exp\left( -\sqrt{\frac{k_B}{D_B}} L \right) - \beta \right]}{D_C} \frac{\left[ \exp\left( \sqrt{\frac{k_B}{D_B}} x \right) - \exp\left( -\sqrt{\frac{k_B}{D_B}} x \right) \right]}{\left[ \exp\left( \sqrt{\frac{k_B}{D_B}} L \right) + \exp\left( -\sqrt{\frac{k_B}{D_B}} L \right) \right]}$$

$$- \frac{D_B}{D_C} B_0 \exp\left( -\sqrt{\frac{k_B}{D_B}} x \right) + \left\{ \frac{\left[ B_0 \sqrt{k_B D_B} \exp\left( -\sqrt{\frac{k_B}{D_B}} L \right) - \beta \right]}{\left[ \exp \sqrt{\frac{k_B}{D_B}} L + \exp\left( -\sqrt{\frac{k_B}{D_B}} L \right) \right]} \frac{2}{D_C} - \frac{\sqrt{k_B D_B}}{D_C} B_0 \right\} x$$

Finally, we specify that $C$ attains a constant value, $C_0$, at $x$=0:

$$C(0) = C_0 = c_2 - \frac{D_B}{D_C} B_0$$

$$c_2 = C_0 + \frac{D_B}{D_C} B_0$$

such that

$$C = C_0 + \frac{D_B}{D_C} B_0 - \sqrt{\frac{D_B}{k_B}} \frac{\left[ B_0 \sqrt{k_B D_B} \exp\left( -\sqrt{\frac{k_B}{D_B}} L \right) - \beta \right]}{D_C} \frac{\left[ \exp\left( \sqrt{\frac{k_B}{D_B}} x \right) - \exp\left( -\sqrt{\frac{k_B}{D_B}} x \right) \right]}{\left[ \exp\left( \sqrt{\frac{k_B}{D_B}} L \right) + \exp\left( -\sqrt{\frac{k_B}{D_B}} L \right) \right]}$$

$$- \frac{D_B}{D_C} B_0 \exp\left( -\sqrt{\frac{k_B}{D_B}} x \right) + \left\{ \frac{\left[ B_0 \sqrt{k_B D_B} \exp\left( -\sqrt{\frac{k_B}{D_B}} L \right) - \beta \right]}{\left[ \exp \sqrt{\frac{k_B}{D_B}} L + \exp\left( -\sqrt{\frac{k_B}{D_B}} L \right) \right]} \frac{2}{D_C} - \frac{\sqrt{k_B D_B}}{D_C} B_0 \right\} x$$

and thus

$$\frac{dC}{dx} = -\frac{\left[B_0\sqrt{k_B D_B}\,\exp\left(-\sqrt{\frac{k_B}{D_B}}L\right)-\beta\right]}{D_C}\frac{\left[\exp\left(\sqrt{\frac{k_B}{D_B}}x\right)+\exp\left(-\sqrt{\frac{k_B}{D_B}}x\right)\right]}{\left[\exp\left(\sqrt{\frac{k_B}{D_B}}L\right)+\exp\left(-\sqrt{\frac{k_B}{D_B}}L\right)\right]}$$

$$+\frac{\sqrt{k_B D_B}}{D_C}B_0\exp\left(-\sqrt{\frac{k_B}{D_B}}x\right)+\frac{\left[B_0\sqrt{k_B D_B}\,\exp\left(-\sqrt{\frac{k_B}{D_B}}L\right)-\beta\right]}{\left[\exp\sqrt{\frac{k_B}{D_B}}L+\exp\left(-\sqrt{\frac{k_B}{D_B}}L\right)\right]}\frac{2}{D_C}-\frac{\sqrt{k_B D_B}}{D_C}B_0$$

Therefore, the flux of *C* is given by

$$J_C = -D_C\frac{dC}{dx} = \left[B_0\sqrt{k_B D_B}\,\exp\left(-\sqrt{\frac{k_B}{D_B}}L\right)-\beta\right]\frac{\left[\exp\left(\sqrt{\frac{k_B}{D_B}}x\right)+\exp\left(-\sqrt{\frac{k_B}{D_B}}x\right)\right]}{\left[\exp\left(\sqrt{\frac{k_B}{D_B}}L\right)+\exp\left(-\sqrt{\frac{k_B}{D_B}}L\right)\right]}$$

$$-\sqrt{k_B D_B}B_0\exp\left(-\sqrt{\frac{k_B}{D_B}}x\right)-2\frac{\left[B_0\sqrt{k_B D_B}\,\exp\left(-\sqrt{\frac{k_B}{D_B}}L\right)-\beta\right]}{\left[\exp\sqrt{\frac{k_B}{D_B}}L+\exp\left(-\sqrt{\frac{k_B}{D_B}}L\right)\right]}+\sqrt{k_B D_B}B_0$$

As expected, the flux of *C* at *x*=0 is

$$J_C\big|_{x=0} = -D_C\frac{dC}{dx}\bigg|_{x=0} = \left[B_0\sqrt{k_B D_B}\,\exp\left(-\sqrt{\frac{k_B}{D_B}}L\right)-\beta\right]\frac{[1+1]}{\left[\exp\left(\sqrt{\frac{k_B}{D_B}}L\right)+\exp\left(-\sqrt{\frac{k_B}{D_B}}L\right)\right]}$$

$$-\sqrt{k_B D_B}B_0-2\frac{\left[B_0\sqrt{k_B D_B}\,\exp\left(-\sqrt{\frac{k_B}{D_B}}L\right)-\beta\right]}{\left[\exp\sqrt{\frac{k_B}{D_B}}L+\exp\left(-\sqrt{\frac{k_B}{D_B}}L\right)\right]}+\sqrt{k_B D_B}B_0 = 0$$

Similarly, the flux of *C* at *x*=L is

$$J_C\big|_{x=L} = -D_C \left.\frac{dC}{dx}\right|_{x=L} = \sqrt{k_B D_B} B_0 - 2\frac{\left[B_0\sqrt{k_B D_B}\exp\left(-\sqrt{\frac{k_B}{D_B}}L\right)-\beta\right]}{\left[\exp\sqrt{\frac{k_B}{D_B}}L+\exp\left(-\sqrt{\frac{k_B}{D_B}}L\right)\right]}-\beta$$

We can verify that the flux of $B$ at $x$=0 equals the sum of the flux of $C$ at $x$=$L$ and the flux of $B$ at $x$=$L$:

$$J_B(0) = \sqrt{k_B D_B} B_0 - 2\frac{\left[B_0\sqrt{k_B D_B}\exp\left(-\sqrt{\frac{k_B}{D_B}}L\right)-\beta\right]}{\left[\exp\left(\sqrt{\frac{k_B}{D_B}}L\right)+\exp\left(-\sqrt{\frac{k_B}{D_B}}L\right)\right]}$$

$$J_B(L) = \beta$$

Finally, the flux of $A$ at $x$=0 must be equal and opposite to the flux of $B$ at $x$=0, such that

$$= \sqrt{k_B D_B} B_0 - 2\frac{\left[B_0\sqrt{k_B D_B}\exp\left(-\sqrt{\frac{k_B}{D_B}}L\right)-\beta\right]}{\left[\exp\left(\sqrt{\frac{k_B}{D_B}}L\right)+\exp\left(-\sqrt{\frac{k_B}{D_B}}L\right)\right]} = D_A m$$

$$m = \frac{\sqrt{k_B D_B}}{D_A} B_0 - \frac{2}{D_A}\frac{\left[B_0\sqrt{k_B D_B}\exp\left(-\sqrt{\frac{k_B}{D_B}}L\right)-\beta\right]}{\left[\exp\left(\sqrt{\frac{k_B}{D_B}}L\right)+\exp\left(-\sqrt{\frac{k_B}{D_B}}L\right)\right]}$$

And the concentration profile of $A$ is given by

$$A = A_0 + \left\{ \frac{\sqrt{k_B D_B}}{D_A} B_0 - \frac{2}{D_A} \frac{\left[ B_0 \sqrt{k_B D_B} \exp\left( -\sqrt{\frac{k_B}{D_B}} L \right) - \beta \right]}{\left[ \exp\left( \sqrt{\frac{k_B}{D_B}} L \right) + \exp\left( -\sqrt{\frac{k_B}{D_B}} L \right) \right]} \right\} x$$

The (constant) flux of $A$ is given by

$$J_A = -D_A \frac{dA}{dx} = \frac{\sqrt{k_B D_B}}{D_A} B_0 - \frac{2}{D_A} \frac{\left[ B_0 \sqrt{k_B D_B} \exp\left( -\sqrt{\frac{k_B}{D_B}} L \right) - \beta \right]}{\left[ \exp\left( \sqrt{\frac{k_B}{D_B}} L \right) + \exp\left( -\sqrt{\frac{k_B}{D_B}} L \right) \right]}$$

The total concentration profile is then given by

$$\begin{aligned} Total &= A + B + C \\ &= A_0 + C_0 + \frac{D_B}{D_C} B_0 + \left( 1 - \frac{D_B}{D_C} \right) B_0 \exp\left( -\sqrt{\frac{k_B}{D_B}} x \right) \\ &+ \left( 1 - \frac{D_B}{D_C} \right) \frac{\left[ B_0 \sqrt{k_B D_B} \exp\left( -\sqrt{\frac{k_B}{D_B}} L \right) - \beta \right]}{\sqrt{k_B D_B}} \frac{\left[ \exp\left( \sqrt{\frac{k_B}{D_B}} x \right) - \exp\left( -\sqrt{\frac{k_B}{D_B}} x \right) \right]}{\left[ \exp\left( \sqrt{\frac{k_B}{D_B}} L \right) + \exp\left( -\sqrt{\frac{k_B}{D_B}} L \right) \right]} \\ &+ \left( \frac{1}{D_C} - \frac{1}{D_A} \right) \left\{ 2 \frac{\left[ B_0 \sqrt{k_B D_B} \exp\left( -\sqrt{\frac{k_B}{D_B}} L \right) - \beta \right]}{\left[ \exp \sqrt{\frac{k_B}{D_B}} L + \exp\left( -\sqrt{\frac{k_B}{D_B}} L \right) \right]} - \sqrt{k_B D_B} B_0 \right\} x \end{aligned} \qquad (15)$$